Eur. Phys. J. B **8**, 47–56 (1999)

THE EUROPEAN PHYSICAL JOURNAL B

EDP Sciences

Optical study of an untwinned $(Bi_{1.57}Pb_{0.43})Sr_2CaCu_2O_{8+\delta}$ single crystal: ab-plane anisotropy

H.L. Liu[1,a,b], M.A. Quijada[1,c], D.B. Tanner[1], H. Berger[2], and G. Margaritondo[2]

[1] Department of Physics, University of Florida, Gainesville, FL 32611, USA
[2] Institut de Physique Appliquée, École Polytechnique Fédérale de Lausanne, PHB Ecublens, 1015 Lausanne, Switzerland

Received 16 July 1998

Abstract. We report on the *ab*-plane polarized reflectance of an untwinned $(Bi_{1.57}Pb_{0.43})Sr_2CaCu_2O_{8+\delta}$ single crystal over the frequency range from 80 to 32 000 cm^{-1} (10 meV–4 eV) at temperatures between 10 and 300 K. We find a clear anisotropy in the *ab*-plane optical conductivity above and below T_c, which is very similar to that formerly published data of $Bi_2Sr_2CaCu_2O_8$ (M.A. Quijada *et al.*, Z. Phys. B **94**, 255 (1994)). We employ both the one-component and two-component analyses to the optical data, which suggest that the normal-state infrared anisotropy of $(Bi_{1.57}Pb_{0.43})Sr_2CaCu_2O_{8+\delta}$ originates not only from the mass anisotropy, but also from the scattering rate anisotropy. Our results provide evidence that the electronic structures within the CuO_2 plane are anisotropic. In the superconducting state, there is a definite *ab*-plane anisotropy to the far-infrared absorption. This anisotropy could be due either to anisotropy of the superconducting gap or to anisotropy of the mid-infrared component to the conductivity. We also observe the superconducting condensate is anisotropic: The value of the superconducting penetration depth in the *a*-direction is slightly smaller than that along the *b*-axis.

PACS. 74.25.Gz Optical properties – 74.72.Hs Bi-based cuprates – 78.30.-j Infrared and Raman spectra

1 Introduction

It is generally agreed that the most important element of the high-T_c cuprate superconductors is the two-dimensional CuO_2 plane. The *ab*-plane anisotropy within the CuO_2 plane is a subject of continued interest. Early on most experimental measurements, such as dc resistivity [1–3], the infrared conductivity [4–10], and the penetration depth [11], were performed on single-domain $YBa_2Cu_3O_{7-\delta}$ (Y123). Much of the observed anisotropy in Y123 can be attributed to the quasi-one-dimensional CuO chains; their presence prevents determining whether the CuO_2 planes themselves are intrinsically anisotropic or not. In contrast, $Bi_2Sr_2CaCu_2O_8$ (Bi-2212) provides a better opportunity to study the *ab*-plane anisotropy because there are no chains in these Bi-based compounds.

Previous optical studies have shown that the *ab*-plane polarized reflectance in Bi-2212 is anisotropic above and below T_c [12,13], suggesting there are two important issues about the anisotropy: the anisotropy of the two-dimensional electronic structure in the normal state and the anisotropy of the superconducting order parameter. Transport measurements indicated that the *ab*-plane dc resistivity is anisotropic in Bi-2212 as well [14,15]. Recent angle-resolved photoemission spectroscopy (ARPES) provided evidence for the in-plane anisotropic Fermi surface of Bi-2212 [16,17]. Below T_c, results of ARPES showed that the magnitude of the superconducting gap on different parts of the Fermi surface is different. Indeed, the *ab*-plane anisotropy of the superconducting gap in Bi-2212 has also been confirmed by other experimental measurements including tunneling [18] and Raman scattering [19].

Despite these extensive spectroscopic studies, questions still exist regarding the presence of the structural superlattice along the *b*-axis in Bi-2212, which necessarily affects the observed *ab*-plane anisotropic properties. This gives us a motivation to study Pb-doped Bi-2212 since the superlattice modulation disappears (or changes) gradually as bismuth is replaced by lead [20]. In this paper, we report the new measurements of the *ab*-plane polarized reflectance spectra in a $(Bi_{1.57}Pb_{0.43})Sr_2CaCu_2O_{8+\delta}$ (Bi(Pb)-2212) single crystal. Infrared spectroscopy is an effective tool on several aspects of high-T_c superconductors [21,22]. Unlike the surface sensitive technique of ARPES (approximately 15 Å in the cuprates), infrared light probes the bulk properties of the materials. Optical methods provide information on the dynamics of the free carriers, the nature of the charge-transfer and

[a] Present address: Department of Physics, University of Illinois at Urbana-Champaign, Urbana, IL 61801, USA.
[b] e-mail: `liu@uimrl7.mrl.uiuc.edu`
[c] Present address: Code 551, Goddard Space Flight Center, Greenbelt, MD 20771, USA.

low-energy excitations, the superconducting gap (in principle), phonons and other electronic structures. Furthermore, using polarized reflectance measurements we are able to study the optical response along the principal axes of the crystal. We focus on the dielectric tensor components (*a- vs. b*-axis) of Bi(Pb)-2212 and compare our data to earlier results of Bi-2212 by Quijada *et al.* [12,13].

2 Experimental

Single-crystal Bi(Pb)-2212 was prepared by a standard flux-growth method [23,24]. The crystal was thin platelet with natural mirror-like *ab* surface and typical dimensions of $2.5 \times 3 \times 0.2$ mm^3. As-grown crystal was used without any annealing. The superconducting transition temperature determined by a dc magnetization measurement gave a T_c onset 80 K with $\Delta T_c = 2$ K. Characterizations of dc resistivity, ac susceptibility, X-ray diffraction, and low-energy electron diffraction (LEED) were also performed on similar samples grown in the same way [25]. Results of X-ray measurements [25] indicated that the modified modulation wavelength along the *b*-axis in Bi(Pb)-2212 increases to about $13|b|$ ($\approx 5|b|$ [26,27] in Bi-2212). Furthermore, the LEED pattern [25] exhibited an almost 1×1 structure for Bi(Pb)-2212, whereas it was a 4.6×1 pattern for Bi-2212, suggesting that Pb really enters into the Bi sites.

The polarized reflectance was measured at near-normal incidence. Far-infrared and mid-infrared measurements were carried out on an Bruker 113v Fourier-transform infrared spectrometer. Wire grid polarizers on polyethylene and AgBr were used in the far- and mid-infrared, respectively. A Perkin-Elmer 16U grating spectrometer was used to measure the spectra in the infrared to the ultraviolet (1 000–32 000 cm^{-1}), using wire grid and dichroic polarizers. The room-temperature polarized reflectance in the visible frequency region (14 300–23 800 cm^{-1}) was also measured using a Zeiss MPM 800 Microscope Photometer with grating monochrometer, especially designed for spot measurements. We measured on the shiny, smooth, and well-reflecting spots with a size about 50×50 μm^2 by using a magnification of $10\times$ and $20\times$. For low-temperature measurements, the sample was mounted in a continuous flow helium cryostat. Calibration of the absolute value of the reflectance was done by coating the sample with a 2 000 Å film of aluminum after measuring the uncoated sample. The spectra of the uncoated sample were then divided by the obtained spectrum of the coated sample and corrected for the known reflectance of aluminum. The accuracy in the absolute reflectance is estimated to be $\pm1\%$ and the accuracy of the anisotropy of the reflectance (*i.e.* the difference between *a* and *b* results on the same sample at the same temperature) is better than $\pm0.25\%$.

The optical properties (*i.e.* the complex conductivity $\sigma(\omega) = \sigma_1(\omega) + i\sigma_2(\omega)$ or dielectric function $\epsilon(\omega) = 1 + 4\pi i\sigma(\omega)/\omega$) were calculated from Kramers-Kronig analysis of the reflectance data [28]. Because a large frequency region was covered, Kramers-Kronig analysis would provide reasonably accurate values for the optical constants. To perform these transformations one needs to extrapolate the reflectance at both low and high frequencies. At low frequencies the extension was done by modeling the reflectance using the Drude-Lorentz model and using the fitted results to extend the reflectance below the lowest frequency measured in the experiment. Between the highest-frequency data point and 40 eV, the reflectance was merged with the Bi-2212 results of Terasaki *et al.* [29]; beyond this frequency range a free-electron-like behavior of ω^{-4} was used.

3 Results and discussion

3.1 Polarized reflectance

In Figure 1 we show the comparison of the room-temperature polarized reflectance of Bi(Pb)-2212 and Bi-2212 [12,13] over a wide frequency range. The anisotropy features of the optical spectra for both materials look very similar: first, the *a*-axis reflectance is higher than the *b*-axis reflectance by 1–2% in the far-infrared region. As the frequency increases, the reflectance falls off in both polarizations; second, the position of the plasma edge for the *b*-axis polarization occurs at slightly lower frequency than in the *a*-axis direction. The splitting is estimated to be around 500 cm^{-1}; and third, the reflectance is substantially higher along the *b*-axis above the plasma minimum. However, there are some differences between the spectra as well. As seen in Figure 1, the absorption band of Bi-2212 at ~ 3.8 eV is more pronounced along *b*- than in the *a*-direction. The difference is smaller in Bi(Pb)-2212.

We emphasize that the *ab*-plane anisotropy of polarized reflectance spectra is not due to inhomogeneity of high-T_c samples parallel to the *c*-axis. Such inhomogeneity could result in surface steps with different structure or composition. In all measurements, we examined on shiny, smooth, and well-reflecting surfaces. The data were reproducibly observed at three different spots on the sample in the visible frequency range by using microscope measurements. Similar polarization dependence has been reported in earlier ellipsometric measurements of Bi-2212 [30], with a transition at ~ 3.8 eV stronger and sharper for electric field polarized along the modulation direction. The *ab*-plane anisotropy has also been observed in the far-infrared transmittance of free standing Bi-2212 single crystals [31].

3.2 Optical conductivity

The Kramers-Kronig transformation of the polarized reflectance data in Bi(Pb)-2212 yields the real part of the optical conductivity $\sigma_1(\omega)$ shown in Figure 2 at several temperatures. For both polarizations, as T is lowered from room temperate to just above T_c, we observe a sharpening and an increase of the far-infrared conductivity, on account of the increasing dc conductivity. The $\sigma_1(\omega)$ has a frequency dependence that decays much more slowly

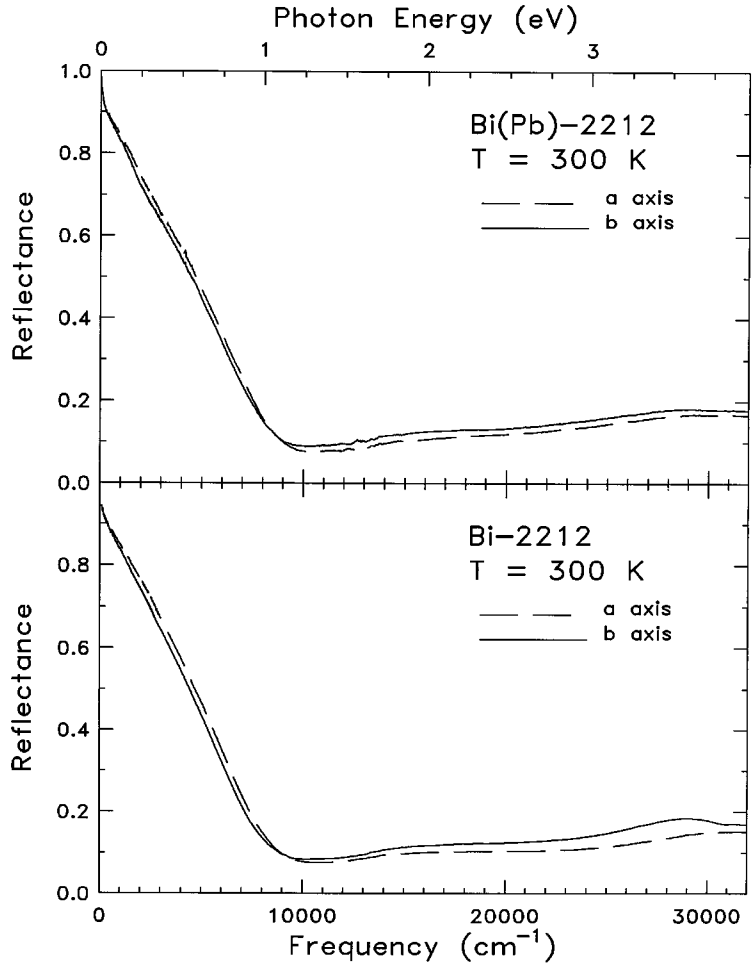

Fig. 1. The room-temperature reflectance of $(Bi_{1.57}Pb_{0.43})Sr_2CaCu_2O_{8+\delta}$ and $Bi_2Sr_2CaCu_2O_8$ [12] over the entire frequency range for light polarized along the a- and b-axes.

than the ω^{-2} expected for a material having a Drude response. This non-Drude behavior, which is universal in the optical conductivity of the copper-oxide superconductors, has been the subject of considerable discussion and controversy [21,22]. Upon entering into the superconducting state, the far-infrared conductivity falls rapidly to a value well below the normal-state value. The missing-area below T_c is a effect of the condensation of the free carriers into the superconducting pairs. At 10 K, there remains a finite conductivity at low frequencies, suggesting no sign of a superconducting gap.

As can be seen in Figure 2, the anisotropy in the normal-state conductivity is about 10%, with the far-infrared conductivity higher in the a-direction. Below T_c, there is a considerably larger far-infrared conductivity along the b-axis down to $\sim$ 20 meV. The ab-plane anisotropic behavior of $\sigma_1(\omega)$ from electronic contributions in Bi(Pb)-2212 is very similar to that observed in Bi-2212 [12,13]. However, there are some differences in the vibrational structures between two materials. In Bi(Pb)-2212, the 640 cm^{-1} phonon mode is visible along the a- and b-axes, but stronger in the b-direction in the whole measured temperature range. By contrast, the phonon mode around 630 cm^{-1} in Bi-2212 splits into two peaks along the b-axis [12,13]. This difference demonstrates that Bi(Pb)-2212 is less structurally anisotropic.

3.3 Oscillator strength sum rule

It is instructive to quantify the anisotropic spectral weight by integrating the optical conductivity from zero to a certain frequency $\hbar\omega$. Based on the conductivity data, we define the partial sum rule, $(m/m^*)N_{eff}(\omega)$ as [28]

$$\left[\frac{m}{m^*}\right] N_{eff}(\omega) = \frac{2mV_{cell}}{\pi e^2 N_{\rm Cu}} \int_0^{\omega} \sigma_1(\omega')d\omega', \qquad (1)$$

where m^* is the effective mass of the carriers, m is the free-electron mass, V_{cell} is the unit cell volume, and $N_{\rm Cu}$ is the number of CuO layers per unit cell. Here, we use $N_{\rm Cu} = 2$ for Bi(Pb)-2212. $(m/m^*)N_{eff}(\omega)$ is proportional to the number of carriers involved in optical excitations up to $\hbar\omega$.

In Figure 3 we plot the room-temperature results for $(m/m^*)N_{eff}(\omega)$ per planar Cu atom along a- and

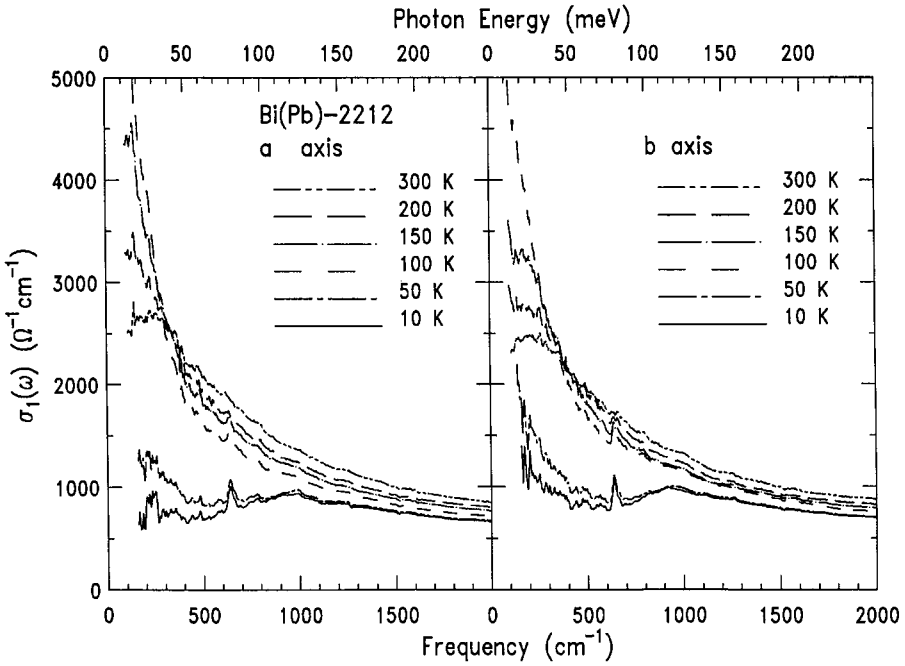

Fig. 2. Left panel: temperature dependence of the a-axis optical conductivity obtained from Kramers-Kronig analysis of the reflectance spectra of $(Bi_{1.57}Pb_{0.43})Sr_2CaCu_2O_{8+\delta}$. Right panel: results for the b-axis.

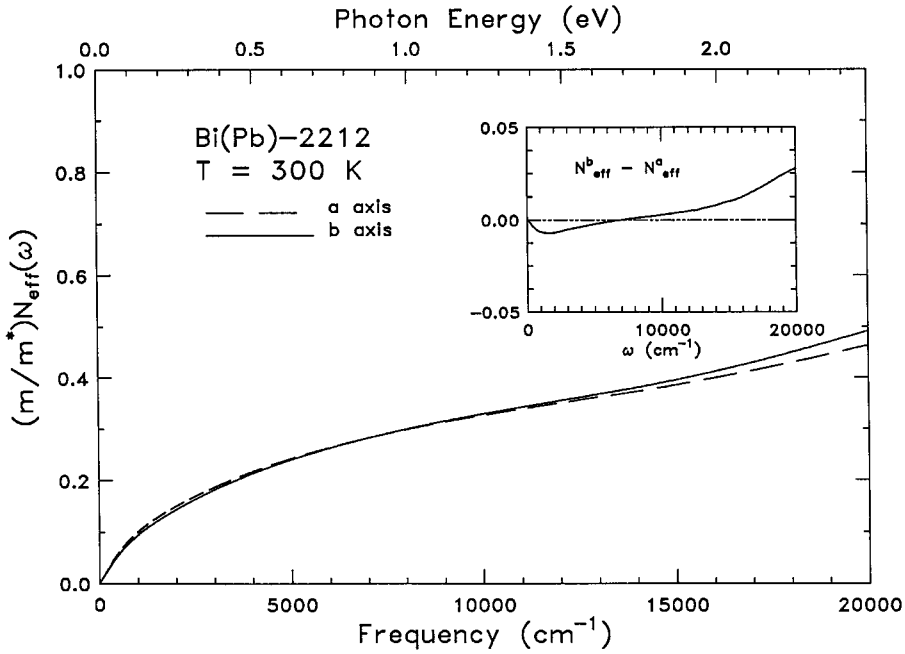

Fig. 3. The room-temperature effective number of carriers per planar Cu atom for polarization along a- and b-axes of $(Bi_{1.57}Pb_{0.43})Sr_2CaCu_2O_{8+\delta}$, obtained from an integration of the conductivity using equation (1). The inset shows the difference of effective carrier numbers between two polarizations.

b-axes. The inset of Figure 3 shows the difference of $(m/m^*)N_{eff}(\omega)$ for two polarizations. We first notice that $(m/m^*)N_{eff}(\omega)$ shares some common features along both directions. It rises rapidly at low frequencies due to a Drude-like band peaked at $\omega = 0$, and begins to level off near 8 000 cm^{-1}, then rises again above the onset of the charge-transfer band. Interestingly, the difference of $(m/m*)N_{eff}(\omega)$ shows that there is more spectral weight ($\omega < 5\,000$ cm^{-1}) in the a-direction. With increasing frequency, two $(m/m^*)N_{eff}(\omega)$ curves come together around 8 000 cm^{-1}. Differences appear again at higher energies; in particular the b-axis value is higher than the a-axis value.

We also find that the difference of effective carriers number between two polarizations is small below 8 000 cm^{-1}, but becoming larger at higher frequencies.

3.4 Dielectric function models

Two approaches are usually considered in analyzing infrared data of superconducting cuprates. The first assumes as a single type of carrier with a frequency-dependent scattering rate due to coupling between the carriers and optically inactive excitation, such as spin excitations. The second takes there to be two sets of charge carriers, a Drude contribution centered at $\omega = 0$ and a second mid-infrared absorption band arising from bound charges such as interband transitions.

3.4.1 One-component model

We first consider the single-component picture by using the marginal Fermi liquid (MFL) theory of Varma *et al.* [32,33], and the nested Fermi liquid (NFL) theory of Virosztek *et al.* [34,35]. In these models, the dielectric function is

$$\epsilon(\omega) = \epsilon_\infty - \frac{\omega_p^2}{\omega[\omega - 2\Sigma(\omega/2)]} \tag{2}$$

with the self-energy of the charge carriers (essentially the scattering rate) taking the form,

$$-\text{Im } \Sigma(\omega, T) \sim \begin{cases} \pi^2 \lambda_T T, & \omega < T \\ \pi \lambda_\omega \omega, & \omega > T \end{cases} \tag{3}$$

where ω_p is the bare plasma frequency, ϵ_∞ is the high frequency limit of $\epsilon(\omega)$, and λ_T or λ_ω is a dimensionless coupling constant. Hence, for $\omega < T$ the model predicts a renormalized scattering rate that is linear in temperature, which is expected from the linear temperature dependence in the resistivity. As ω increases, reaching a magnitude of order of T, evidence of interactions with a new spectrum of excitations arises. This causes $-\text{Im } \Sigma(\omega, T)$ to grow linearly with frequency up to a cutoff frequency ω_c that is introduced in the model. The real part of Σ is related to the effective mass m^* of the interacting carriers by $m^*(\omega)/m = 1 - 2\text{Re } \Sigma(\omega/2)/\omega$ whereas the imaginary part of Σ is related to the quasiparticle lifetime through $1/\tau^*(\omega) = -2m\,\text{Im } \Sigma(\omega/2)/m^*(\omega)$.

Figures 4 and 5 show the imaginary part of the self energy $-\text{Im } \Sigma(\omega, T)$ and effective mass enhancement $m^*(\omega)/m$ of Bi(Pb)-2212 at several temperatures and along a- and b-axes. We estimate the values of ω_p from the conductivity sum-rule analysis in equation (1), integrating $\sigma_1(\omega)$ up to the charge-transfer band. The value for ϵ_∞ are obtained by fitting the reflectance data using a Drude-Lorentz model. The actual values of ω_p and ϵ_∞ are 17 870 cm^{-1} and 3.6 for the a-axis; 18 100 cm^{-1} and 3.9 for the b-axis, respectively.

The MFL analysis in Figure 4 has two interesting results. First, for two polarizations the frequency-dependent imaginary part of the self-energy has a linear-in-ω dependence up to frequency of 1 000 cm^{-1}. Second, the $-\text{Im } \Sigma(\omega, T)$ is different between the a- and b-axes. We can simply write the imaginary part of the self energy as a sum of three terms: $1/\tau_0 + 1/\tau(\omega) + 1/\tau(T)$, where the first term stands for the impurity scattering, the second and third terms for the ω and T dependence, respectively. We take difference between $-\text{Im } \Sigma(\omega, T)$ for the a- and b- polarizations and find that the enhanced scattering rate along the b-axis is mainly attributed to an increase of $1/\tau_0$ by 100–150 cm^{-1}, while the frequency- and temperature-dependent contribution is small. Moreover, we estimate the slope of $-\text{Im } \Sigma(\omega, T)$ between 200 cm^{-1} and 1 000 cm^{-1} at 300 K, which yields a coupling constant $\lambda_\omega^a \sim 0.28$ and $\lambda_\omega^b \sim 0.30$. This result suggests that the coupling between the charge carriers and whatever excitation which dominates the linear scattering rate has tensor components.

As expected for the MFL picture, the effective mass, shown in Figure 5, is enhanced at low frequencies, and then drops off to equal the bare electron mass at high frequencies. This also means that an increase of $m^*(\omega)/m$ results in a decrease of $-\text{Im } \Sigma(\omega, T)$ at low frequencies (see Fig. 4) since heavy carriers are more difficult to scatter. It is clearly seen in Figure 5 that the mass enhancement at low frequencies is anisotropic, on account of the small difference in the values of ω_p. At room temperature, the extrapolated $[m^*(\omega = 0)/m] \sim 2$ is comparable to that of $m^* \sim 2m$ calculated from the density functional method of Bi-2212 [36]. The temperature-dependent change of the effective mass is enhanced at lower frequencies by an amount which is largest at lower temperatures.

3.4.2 Two-component picture

We now discuss the two-component approach. In this model, the free carriers are assumed to account for the dc conductivity and far-infrared, T-dependent part of the spectrum while the mid-infrared part accounts for the non-Drude part. The free-carrier component was fit to a Drude model. The mid-infrared and high-energy components were fit by Lorentzian oscillators. The dielectric function is

$$\epsilon(\omega) = -\frac{\omega_{pD}^2}{\omega^2 + i\omega/\tau_D} + \sum_{j=1}^{N} \frac{\omega_{pj}^2}{\omega_j^2 - \omega^2 - i\omega\gamma_j} + \epsilon_\infty \cdot \tag{4}$$

In equation (4), the first term represents the Drude component described by a Drude plasma frequency ω_{pD} and scattering rate $1/\tau_D$; the second term is a sum of mid-infrared and interband oscillators with ω_j, ω_{pj}, and γ_j being the resonant frequency, oscillator strength, and the width of the j^{th} Lorentz oscillator respectively.

The two-component analysis is in accord with two expectations. First, the fitting results indicate that the oscillator strength for the Drude term is nearly temperature independent. We find $\omega_{pD}^a = 9\,000 \pm 200$ cm^{-1} and

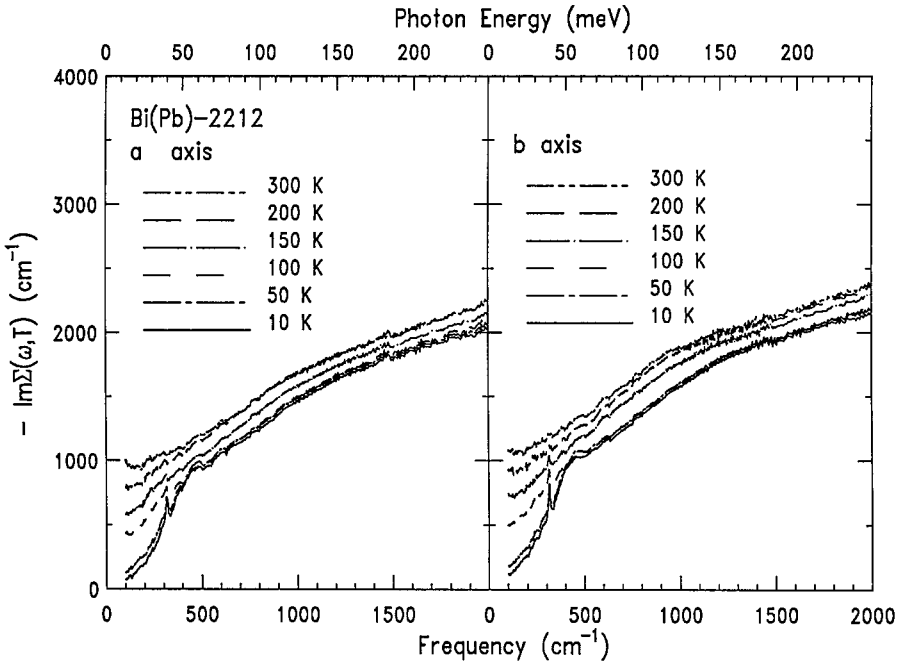

Fig. 4. The imaginary part of the self-energy $-\mathrm{Im}\ \Sigma(\omega, T)$ for $(Bi_{1.57}Pb_{0.43})Sr_2CaCu_2O_{8+\delta}$ obtained from the marginal Fermi liquid theory in equation (2) at several temperatures and two polarizations.

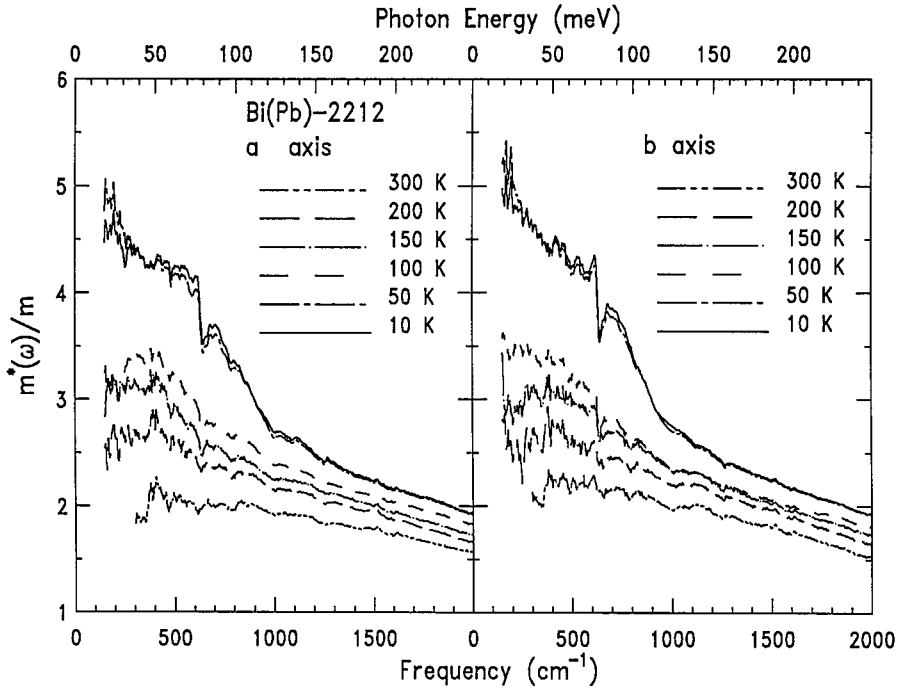

Fig. 5. The frequency-dependent effective mass $m^*(\omega)/m$ at various temperatures for $(Bi_{1.57}Pb_{0.43})Sr_2CaCu_2O_{8+\delta}$.

$\omega_{pD}^b = 8\,600 \pm 200$ cm^{-1}. When $T > T_c$, the scattering rate of the free carrier or Drude contribution has a linear temperature dependence, shown in Figure 6. Such a T-linear behavior in $1/\tau_D$ above T_c was observed previously by infrared measurements [37–39] and is a unique property of the cuprate superconductors. Below T_c, the scattering rate $1/\tau_D$ exhibits a fast drop, suggesting a strong suppression of the scattering channel through the superconducting transition. More significantly, the fitted $1/\tau_D$ shows anisotropic and is larger along the b-axis than the one obtained for the a-axis at each temperature. Writing $\hbar/\tau_D = 2\pi\lambda_D\ k_B T + \hbar/\tau_0$ [40], a straight line fit to the $1/\tau_D$ above T_c gives the coupling constant of $\lambda_D^a \sim 0.29$ and $\lambda_D^b \sim 0.30$, similar to that obtained in the one-component analysis.

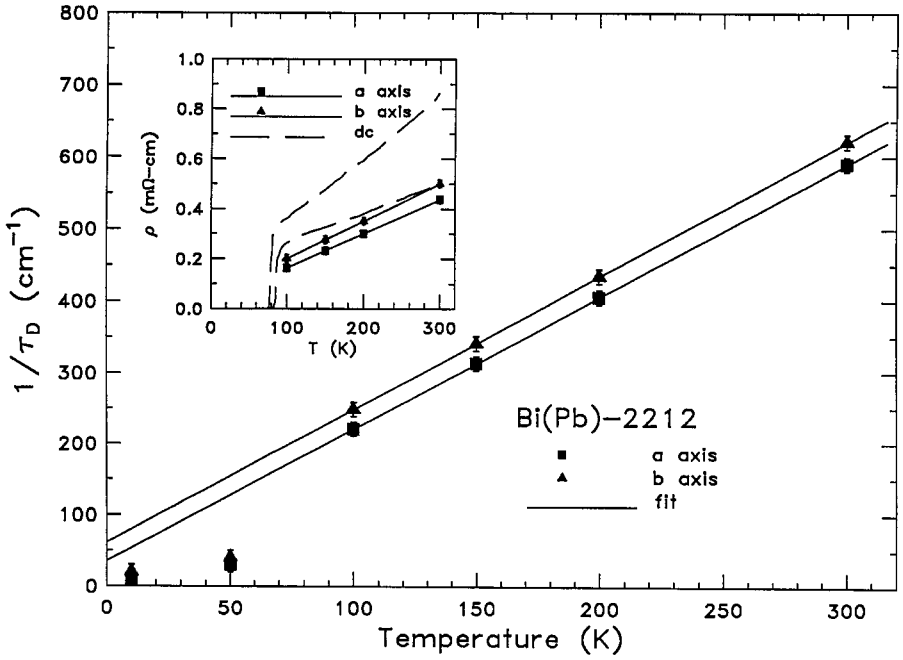

Fig. 6. The zero-frequency scattering rate $1/\tau_D$ (symbols) of the free carrier contribution from the two-component fit of equation (4) to the optical conductivity of $(Bi_{1.57}Pb_{0.43})Sr_2CaCu_2O_{8+\delta}$. The straight line shows a linear fit to the temperature dependence of $1/\tau_D$ above T_c. The inset shows the *ab*-plane anisotropy of the far-infrared resistivity (symbols) deduced from the optical measurements and the averaged *ab*-plane dc transport data (dashed line) [25].

The observed anisotropy of $1/\tau_D$ in Bi(Pb)-2212 can be connected with the dc transport anisotropy. Using the parameters of Drude plasma frequency given above and the temperature dependence of $1/\tau_D$, the far-infrared resistivity is written as $(\rho_{ir} = \left(\omega_{pD}^2\tau_D/60\right)^{-1}$, in units of $\Omega\,\mathrm{cm}$), and is shown in the inset of Figure 6. For comparison, two dc transport data (averaged *ab*-plane) are included [25]. We find that the anisotropy ratio of ρ_{ir}^b/ρ_{ir}^a is 1.15–1.22. This behavior demonstrates that the anisotropy in the far-infrared resistivity of Bi(Pb)-2212 is caused by the anisotropy of the free-carrier relaxation rate combined with the normal-state anisotropy of the Drude plasma frequency. We also notice that the absolute value of averaged *ab*-plane dc resistivity is larger by a factor of as much as 1.8 than our results deduced from the optical measurements. This discrepancy may arise from the differences in oxygen stoichiometry of the Bi(Pb)-2212 samples. Nevertheless, the close agreement in the anisotropy of the resistivity deduced from the optical and transport measurements has been previously observed in Bi-2212 [13].

3.5 Superconducting state

3.5.1 Anisotropy of the ab-plane

As mentioned above, there is a definite anisotropy of the far-infrared conductivity in the superconducting state, shown in Figure 2. The *b*-axis conductivity is larger than the *a*-axis conductivity at 50 and 10 K. The exact value of the observed superconducting-state anisotropy is difficult to quantify partly because the *ab*-plane far-infrared reflectivity is close to unity below T_c. Two possibilities are considered to explain the observed low-frequency anisotropy of $\sigma_1(\omega)$ at $T < T_c$. First, in the one-component picture, the superconducting-state conductivity is due to excitations across the superconducting gap. Hence, the gap must be anisotropic. It was shown by ARPES that the superconducting gap, at least in Bi-2212, is highly anisotropic in *k*-space [41–43]. If this interpretation is adopted, the differences between the *a*- and *b*- directions of optical conductivity in Bi(Pb)-2212 would imply a two-fold symmetry to the superconducting gap absorption. Then, our data is contradictory to most of the experimental results in Bi-2212. It is generally concluded that there is a large gap anisotropy in Bi-2212 which closely mimics the four-fold symmetry of a $d_{x^2-y^2}$ superconducting order parameter [18,19,41–43]. The second possibility is that with the choice of the two-component picture, the observed anisotropy in $\sigma_1(\omega)$ can be attributed to the anisotropy of the mid-infrared conductivity. The anisotropy could then be due to two factors. In the normal state, the free-carrier scattering rate is 14% higher along *b* ($1/\tau_D(100\ K) = 250\ \mathrm{cm}^{-1}$ for the *b*-axis and $220\ \mathrm{cm}^{-1}$ for the *a*-axis). Above and below T_c, the second mid-infrared component has a larger contribution along the *b*-axis than along the *a*-axis.

3.5.2 Superconducting condensate

Although the measured optical data do not by themselves distinguish between the above two possibilities, the *ab*-plane anisotropy of the amount of conductivity that

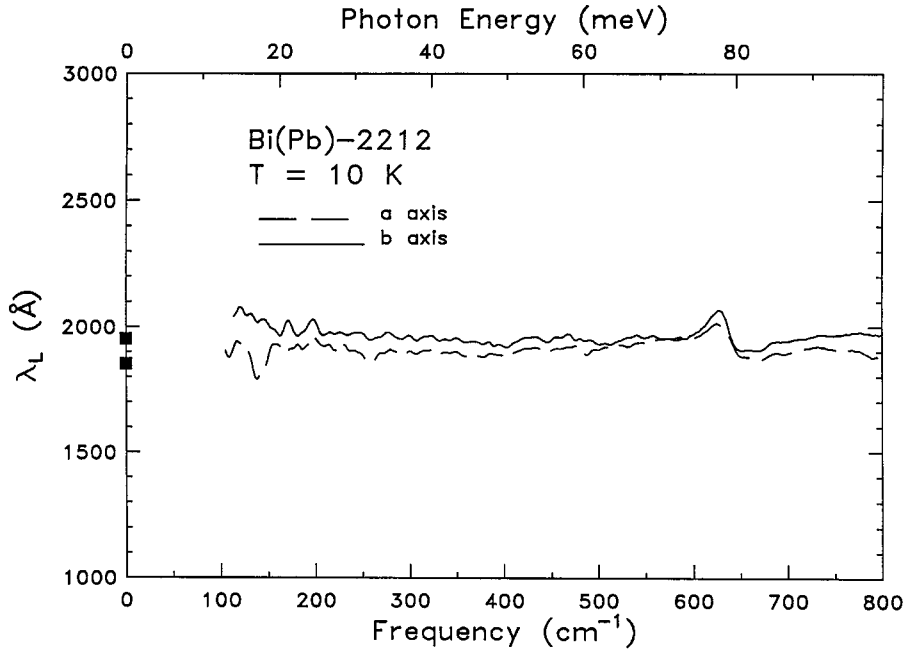

Fig. 7. The *ab*-plane frequency-dependent superconducting penetration depth $\lambda_L(\omega)$ of $(Bi_{1.57}Pb_{0.43})Sr_2CaCu_2O_{8+\delta}$ at 10 K, obtained from equation (6). The values of $\lambda_L(0)$ from the sum-rule analysis of equation (5) are indicated by the symbols.

condenses into the δ function at $\omega = 0$ is given less ambiguously. The missing area can be written in terms of the plasma frequency of superconducting carriers, ω_{pS}, by sum-rule argument:

$$\frac{\omega_{pS}^2}{8} = \int_0^\infty (\sigma_{1n}(\omega) - \sigma_{1s}(\omega))\, d\omega \qquad (5)$$

where $\sigma_{1n}(\omega)$ and $\sigma_{1s}(\omega)$ are the real parts of the complex conductivity at $T \approx T_c$ and $T \ll T_c$, respectively. ω_{pS} is related to superfluid density, n_s, by $\omega_{pS} = \sqrt{4\pi n_s e^2/m^*}$, and also to the superconducting penetration depth, λ_L, by $\lambda_L = c/\omega_{pS}$ where c is the light speed. Evaluation of the integral in equation (5) gives the values of $\omega_{pS}^a = 8\,600 \pm 200$ cm^{-1} and $\omega_{pS}^b = 8\,150 \pm 200$ cm^{-1} in Bi(Pb)-2212 at 10 K. The results indicate the superconducting condensate is larger along the *a*-axis.

The *ab*-plane anisotropy of superfluid density reflects the anisotropy of the superconducting penetration depth. In Figure 7, we plot the frequency dependent penetration depth of Bi(Pb)-2212 along *a*- and *b*-axes at 10 K. This quantity is defined as

$$\lambda_L(\omega) = \left[\frac{c^2}{4\pi\omega\sigma_2(\omega)}\right]^{1/2} \qquad (6)$$

where $\sigma_2(\omega)$ is the imaginary part of the optical conductivity obtained from Kramers-Kronig analysis of the reflectance data. A smaller λ_L would correspond to a larger superfluid density. The fact that both curves in Figure 7 are nearly flat suggests that the primary contribution to $\sigma_2(\omega)$ is from the superfluid carrier response. The extrapolated zero-frequency penetration depth approaches the values obtained by sum-rule analysis (symbols at $\omega = 0$ in Fig. 7), *i.e.* $\lambda_L^a \sim 1\,850$ Å and $\lambda_L^b \sim 1\,950$ Å. We also notice that the values of λ_L^a and λ_L^b in Bi(Pb)-2212 are very close to those in Bi-2212 [13], $\lambda_L^a \sim 1\,800$ Å and $\lambda_L^b \sim 1\,960$ Å. While the anisotropy ratio, $\lambda_L^b/\lambda_L^a \sim 1.05$, in Bi(Pb)-2212 is slightly smaller than that, $\lambda_L^b/\lambda_L^a \sim 1.1$, in Bi-2212.

3.6 Spectral weight above and below T_c

We compare the various electronic contributions to $\sigma_1(\omega)$ in both the normal and superconducting state. We use finite-frequency sum-rule analysis in equation (1) and then calculate the effective number of carriers per planar Cu atom in the low frequency region below the charge-transfer gap ($\omega < 16\,000$ cm^{-1}) as N_{tot}, the Drude or free carrier part (from two-component analysis) as N_{Drude}, and the superconducting condensate weight as N_s. We assume the effective mass to be the free-electron mass. Results for Bi(Pb)-2212 and Bi-2212 [12,13] are summarized in Table 1. We first describe the results of N_{tot} and will discuss others latter. The values of N_{tot}^a and N_{tot}^b in Bi(Pb)-2212 are slightly higher than those in Bi-2212, although N_{tot}^b is always larger than N_{tot}^a in both materials. The slight increase of the total carrier numbers in Bi(Pb)-2212 may be due to the Pb doping or the different oxygen stoichiometry. The differences between N_{tot}^a and N_{tot}^b reflect that the *b*-axis conductivity below the charge-transfer band contains more spectral weight than that in the *a*-direction. The anisotropy ratio of $N_{tot}^b/N_{tot}^a \sim 1.05$ in Bi(Pb)-2212 coincides with the value obtained by Bi-2212. This is remarkable: as the substitution of Pb in Bi-2212 induces

Table 1. Effective number of carriers per planar Cu atom.

Material	$\mathbf{E}_{\parallel}$	N_{tot}	N_{Drude}	N_s	$\frac{N_s}{N_{tot}}\%$	$\frac{N_s}{N_{Drude}}\%$
$(Bi_{1.57}Pb_{0.43})Sr_2CaCu_2O_{8+\delta}$	a	0.40	0.103	0.093	23	90
	b	0.42	0.094	0.084	20	89
$Bi_2Sr_2CaCu_2O_8$	a	0.37	0.105	0.094	25	90
	b	0.39	0.096	0.083	21	86
Typical uncertainties		$\pm.03$	$\pm.01$	$\pm.01$	$\pm1\%$	$\pm4\%$

a new incommensurate modulation periodicity in the b-direction, but does not make a significant change on the anisotropy ratio of the total carriers number (b- *vs.* a-axis) in comparison with that of Bi-2212. Thus, it appears that the origin of the ab-plane anisotropy in Bi(Pb)-2212 is the same as in Bi-2212. Our data provide evidence that the electronic properties of these Bi-based compounds are anisotropic within the CuO_2 plane, regardless of the superstructure in the Bi-O layer.

We discuss the number of effective carriers in the Drude part and the superfluid per copper displayed in Table 1. In Bi(Pb)-2212, the value of N^b_{Drude} is smaller than N^a_{Drude} (the opposite is the case in the total carriers number), and the anisotropic ratio of N^a_{Drude}/N^b_{Drude} is ~ 1.1. In the superconducting state, the anisotropy ratio of N^a_s/N^b_s is $\sim$ 1.1. Notably, the number of free carriers and the number of superconducting carriers are both larger for polarization along a than along b. We also consider the superconducting condensate fraction in Table 1. The superfluid density consumes about 20–25% of the total doping-induced oscillator strength; and about 75–80% remains at finite frequencies for both polarizations. If the two-component picture is adopted, nearly 90% of free-carrier spectral weight condenses to form the superfluid density along the a- and b-axes. These numbers are consistent with the basic clean-limit point of view, that the oscillator strength of the δ function is essentially the same as that of the Drude-like zero-frequency peak of the normal state. The above argument is also true for the behavior of the superfluid density in Bi-2212 [12,13].

4 Summary

In summary, we present the ab-plane polarized reflectance of an untwinned Bi(Pb)-2212 single crystal over a wide frequency range above and below T_c. We find that the far-infrared a-axis reflectance is higher than the b-axis reflectance by 1–2% whereas the reflectance is higher along the b-axis in the visible to ultraviolet region. This anisotropy is very similar to that previously reported in Bi-2212 [12,13]. Our new data suggest that the observed anisotropic behavior of polarized reflectance spectra is an intrinsic property within the CuO_2 plane, irrespective of the superstructure in the Bi-O layer.

The anisotropy in the normal-state conductivity is about 10%, with the far-infrared conductivity higher in the a-polarization. Both one-component and two-component analyses of the optical data show that the overall magnitude of the low-frequency scattering rate and effective mass enhancement is larger along b than those along a. This indicates the normal-state infrared anisotropy of Bi(Pb)-2212 originates not only from the mass anisotropy, but also from the scattering rate anisotropy.

The ab-plane anisotropy observed in the normal-state conductivity persists in the superconducting state as well. Below T_c, there is a definite anisotropy to the far-infrared conductivity, with a considerably larger conductivity along the b axis down to $\sim$ 20 meV. This anisotropy could be due either to anisotropy of the superconducting gap or to anisotropy of the mid-infrared component to the conductivity. Another important finding is that the superfluid response is larger along a than b, corresponding to values of the superconducting penetration depth, $\lambda^a_L \sim 1\,850$ Å and $\lambda^b_L \sim 1\,950$ Å. The oscillator strength of the superfluid contains about 20–25% of the total-doping induced carriers or near 90% of the free-carrier spectral weight in the normal state. This suggests the clean-limit picture resides on the a- and b-polarizations of Bi(Pb)-2212.

This work at University of Florida is supported by National Science Foundation, Grant No. DMR-9705108.

References

1. T.A. Friedmann, M.W. Rabin, J. Giapintzakis, J.R. Rice, D.M. Ginsberg, Phys. Rev. B **42**, 6217 (1990).
2. U. Welp, S. Fleshler, W.K. Kwok, J. Downey, Y. Fang, G.W. Crabtree, J.Z. Liu, Phys. Rev. B **42**, 10189 (1990).
3. R. Gagnon, C. Lupien, L. Taillefer, Phys. Rev. B **50**, 3458 (1994).
4. B. Koch, H.P. Geserich, T. Wolf, Solid State Commun.**71**, 495 (1989).
5. Z. Schlesinger, R.T. Collins, F. Holtzberg, C. Field, S.H. Blanton, U. Welp, G.W. Crabtree, Y. Fang, J.Z. Liu, Phys. Rev. Lett. **65**, 801 (1990).

6. T. Pham, H.D. Drew, S.H. Moseley, J.Z. Liu, Phys. Rev. B **44**, 5377 (1991).
7. L.D. Rotter, Z. Schlesinger, R.T. Collins, F. Holtzberg, C. Field, U. Welp, G.W. Crabtree, J.Z. Liu, Y. Fang, G. Vandervoort, S. Fleshler, Phys. Rev. Lett. **67**, 2741 (1991).
8. S.L. Cooper, A. Kotz, M.A. Karlow, M.V. Kelin, W.C. Lee, J. Giapintzakis, D.M. Ginsberg, Phys. Rev. B **45**, 2549 (1992).
9. S.L. Cooper, D. Reznik, A. Kotz, M.A. Karlow, R. Liu, M.V. Kelin, W.C. Lee, J. Giapintzakis, D.M. Ginsberg, B.W. Veal, A.P. Paulikas, Phys. Rev. B **47**, 8233 (1993).
10. D.N. Basov, R. Liang, D.A. Bonn, W.N. Hardy, B. Dabrowski, M. Quijada, D.B. Tanner, J.P. Rice, D.M. Ginsberg, T. Timusk, Phys. Rev. Lett. **74**, 598 (1995).
11. K. Zhang, D.A. Bonn, S. Kamal, R. Liang, D.J. Baar, W.N. Hardy, D. Basov, T. Timusk, Phys. Rev. Lett. **73**, 2484 (1994).
12. M.A. Quijada, D.B. Tanner, R.J. Kelley, M. Onellion, Z. Phys. B **94**, 255 (1994).
13. M.A. Quijada, Ph.D. thesis, Department of Physics, University of Florida (1994).
14. S. Martin, A.T. Fiory, R.M. Fleming, L.F. Schneemeyer, J.V. Waszczak, Phys. Rev. Lett. **60**, 2194 (1990).
15. K. Yamaya, T. Haga, T. Honma, Y. Abe, F. Minami, S. Takekawa, Y. Tajima, Y. Hidaka, Physica C **162-164**, 1009 (1989).
16. P. Aebi, J. Osterwalder, P. Schwaller, L. Schlapbach, M. Shimoda, T. Mochiku, K. Kadowaki, Phys. Rev. Lett. **72**, 2757 (1994).
17. H. Ding, A.F. Bellman, J.C. Campuzano, M. Randeria, M.R. Norman, T. Yokoya, T. Takahashi, H. Katayama-Yoshida, T. Mochiku, K. Kadowaki, G. Jennings, G.P. Brivio, Phys. Rev. Lett. **76**, 1553 (1996).
18. J. Kane, Q. Chen, K.-W. Ng, Phys. Rev. Lett. **72**, 128 (1994).
19. T.P. Devereaux, A.P. Kampf, Int. J. Mod. Phys. **11**, 2093 (1997), references therein.
20. H. Heinrich, G. Kostorz, B. Heeb, L.J. Gauckler, Physica C **224**, 133 (1994).
21. T. Timusk, D.B. Tanner in *Physical properties of High Temperature Superconductors I*, edited by D.M. Ginsberg (World Scientific, Singapore, 1989) p. 339.
22. D.B. Tanner, T. Timusk, in *Physical Properties of High Temperature Superconductors III,* edited by D.M. Ginsberg (World Scientific Press, 1992) p. 363.
23. P.D. Han, D.A. Payne, *J. Crystal Growth* **104**, 201 (1990).
24. D.B. Mitzi, L.W. Lombardo, A. Kapitulunik, S.S. Laderman, R.D. Jacowitz, Phys. Rev. B **41**, 6564 (1990).
25. Jian Ma, P. Alméras, R.J. Kelly, H. Berger, G. Margaritondo, X.Y. Cai, Y. Feng, M. Onellion, Phys. Rev. B **51**, 9271 (1995).
26. M.D. Kirk, J. Nogami, A.A. Baski, D.B. Mittzi, A. Kapitulnik, T.H. Geballe, C.F. Quate, Science **242**, 1673 (1988).
27. R.M. Hazen, in *Physical Properties of High Temperature Superconductors II,* edited by D.M. Ginsberg (World Scientific Press, 1990) p. 129.
28. F. Wooten, in *Optical Properties of Solids* (Academic, New York, 1972)
29. I. Terasaki, S. Tajima, H. Eisaki, H. Takagi, K. Uchinokura, S. Uchida, Phys. Rev. B **41**, 865 (1990).
30. M.K. Kelly, P. Barboux, J.-M. Tarascon, D.E. Aspnes, P.A. Morris, W.A. Bonner, Physica C **162–164**, 1123 (1989).
31. D.B. Romero, G.L. Carr, D.B. Tanner, L. Forro, D. Mandrus, L. Mihaly, G.P. Williams, Phys. Rev. B **44**, 2818 (1991).
32. C.M. Varma, P.B. Littlewood, S. Schmitt-rink, E. Abrahams, A.E. Ruckenstein, Phys. Rev. Lett. **63**, 1996 (1989).
33. P.B. Littlewood, C.M. Varma, J. Appl. Phys. **69**, 4979 (1991).
34. A. Virosztek, J. Ruvalds, Phys. Rev. B **42**, 4064 (1990).
35. C.T. Rieck, W.A. Little, J. Ruvald, A. Virosztek, Phys. Rev. B **51**, 3772 (1995).
36. C.G. Olson, R. Liu, D.W. Lynch, R.S. List, A.J. Arko, B.W. Veal, Y.C. Chang, P.Z. Jiang, A.P. Paulikas, Phys. Rev. B **42**, 381 (1990).
37. K. Kamarás, S.L. Herr, C.D. Porter, N. Tache, D.B. Tanner, S. Etemad, T. Venkatesan, E. Chase, A. Inam, X.D. Wu, M.S. Hegde, B. Dutta, Phys. Rev. Lett. **64**, 84 (1990).
38. D.B. Romero, C.D. Porter, D.B. Tanner, L. Forro, D. Mandrus, L. Mihaly, G.L. Carr, G.P. William, Phys. Rev. Lett. **68**, 1590 (1992).
39. F. Gao, D.B. Romero, D.B. Tanner, J. Talvacchio, M.G. Forrester, Phys. Rev. B **47**, 1036 (1993).
40. P.B. Allen, T.P. Beaulac, F.S. Khan, W.H. Butler, F.J. Pinski, J.C. Swihart, Phys. Rev. B **34**, 4331 (1986).
41. Jian Ma, C. Quitmann, R.J. Kelly, H. Berger, G. Margaritondo, M. Onellion, Science **267**, 862 (1995).
42. T. Yokoya, T. Takahashi, T. Mochiku, K. Kadpwaki, Phys. Rev. B **53**, 14055 (1996).
43. H.Ding, M.R. Norman, J.C. Campuzano, M. Randeria, A.F. Bellman, T. Yokaya, T. Takahashi, T. Mochiku, K. Kadowaki, Phys. Rev. B **54**, 9678 (1996).